Physics-Informed Broadband Noise Source Identification and Prediction of an Ideally Twisted Rotor

Christopher S. Thurman*, Nikolas S. Zawodny†, Nicole A. Pettingill‡, Leonard V. Lopes§
NASA Langley Research Center, Hampton, VA, 23681

James D. Baeder¶
University of Maryland, College Park, Maryland, 20742

This work aims to provide a physics-based approach for the prediction and isolation of broadband noise emanating from different regions of an ideally twisted rotor. A preliminary prediction was conducted using a lattice-Boltzmann method–very-large-eddy simulation (LBM-VLES) implemented within the software suite, PowerFLOW. Regions of particular interest to broadband noise were investigated by calculating one-third octave sound pressure levels of the unsteady pressure fluctuations acting on the rotor. These regions were then treated as individual Ffowcs Williams and Hawkings (FW-H) surfaces and simulated for three run conditions at a finer spatial resolution to identify the broadband noise from these separate regions and isolate it from the total acoustic spectra. These predictions were then compared to experimentally acquired data and to semiempirical prediction methods to highlight the acoustic contributions of various broadband noise generation mechanisms as well as to exemplify and explain shortcomings in the semiempirical methodology.

Nomenclature

Ω	=	Rotor rotational rate, revolutions per minute (RPM)
R	=	Rotor tip radius, inches
θ_0	=	Collective pitch measured from root, deg.
θ_t	=	Blade tip pitch, deg.
M_t	=	Tip Mach number, dimensionless
c	=	Rotor chord length, inches
SPL	=	Sound pressure level, dB
$SPL_{1/3}$	=	One-third octave sound pressure level, dB
PSD	=	Power spectral density, dB/Hz
ϕ	=	Observer angle relative to rotor plane, deg.
$y+$	=	Normalized wall distance, dimensionless
Δ	=	Vortex miss distance, dimensionless

I. Introduction

Over the past decade, there has been a considerable increase in the demand and usage of small unmanned aerial systems (sUAS). These sUAS vehicles have shown great potential for applications such as package delivery and aerial surveillance due to their relatively small size and maneuvering capabilities. The difference in size of these sUAS vehicles, when compared to traditional helicopters, has shown somewhat of a paradigm shift in the relative importance of different noise generating mechanisms. For example, it has been shown that the stochastic, or broadband, portion of the noise emanating from such sUAS vehicles lies in the most perceptible range of human audibility and is a dominant

*Research Aerospace Engineer, Aeroacoustics Branch, 2 N. Dryden St. MS 461, AIAA Member; christopher.thurman@nasa.gov
†Research Aerospace Engineer, Aeroacoustics Branch, 2 N. Dryden St. MS 461, AIAA Member; nikolas.s.zawodny@nasa.gov
‡Research Aerospace Engineer, Aeroacoustics Branch, 2 N. Dryden St. MS 461, AIAA Member; nicole.a.pettingill@nasa.gov
§Senior Research Aerospace Engineer, Aeroacoustics Branch, 2 N. Dryden St. MS 461; leonard.v.lopes@nasa.gov
¶Professor, Department of Aerospace Engineering, 3154 Glenn L. Martin Hall, College Park, MD 20742, AIAA Associate Fellow; baeder@umd.edu

noise source when compared to the deterministic, or tonal, noise [1, 2]. This is in contrast to traditional helicopters where tonal noise dominates over broadband and, for this reason, limited work has been done in the prediction and analysis of this broadband noise until recently.

A semiempirical prediction methodology for broadband noise was devised in Refs. [3, 4] and has been used to some degree of accuracy in Refs. [1, 4–6]. Though these methods provide valuable insight into the different broadband self-noise generating mechanisms, they lack the ability to capture more complex aerodynamically induced noise generation associated with rotorcraft such as atmospheric turbulence ingestion noise (TIN) [7] and blade wake interaction (BWI) noise [8]. This is due to these techniques having been developed based upon a wind tunnel campaign of various fixed, 2D and 3D NACA 0012 airfoil sections.

Higher fidelity predictions using computational simulations have also been used in Refs. [1, 9, 10]; however, these studies focused on total noise prediction. Work was done by the author in Ref. [2] to predict the broadband noise contribution to the total acoustic spectra using periodic extraction techniques devised in Ref. [1]. The post-processing techniques used in Refs. [2, 11] were shown to provide valuable insight in determining regions of the rotor blades responsible for broadband noise generation mechanisms.

The research entailed in this paper aims at not only the broadband noise prediction of an sUAS rotor, but also at the isolation of various broadband noise sources using an a priori simulation to determine and separate various regions along the rotor blades responsible for these different noise sources. Simulations were then conducted using this split geometry to delineate the acoustic contributions from these various regions. The physical insights gained through these simulations were also used to devise a physics-informed strategy for implementing the semiempirical prediction methodology formulated by Brooks, et al. [3]. This new physics-informed strategy takes into account the secondary aerodynamic effects of the tip vortex generation on the outermost part of the rotor blade, as well as the transitional flow characteristics along the span of the blade, to provide more accurate predictions when compared with experimentally measured acoustic data.

II. Technical Approach

A multifaceted, computational strategy entailing the use of various prediction software of varying fidelity was used throughout this work to predict the aerodynamics and aeroacoustics of an ideally twisted rotor in hover. Figure 1 shows the geometry, which was taken from concurrent work performed in Ref. [12]. The rotor had a radius of $R = 6.25$ inches and a constant blade chord of $c = 1.25$ inches. The rotor blades consisted of NACA 0012 airfoils with a modified trailing edge geometry that had a uniform, 0.5 mm thickness along the entire blade span. This rotor geometry was designed to induce uniform inflow and produce 2.5 lb of thrust at a nominal run condition of $\Omega = 5500$ RPM using Blade Element Momentum Theory (BEMT) [13] over the outboard 80% of the span without including tip loss effects. The intent of using this rotor was to take an analytically based approach, which allowed for a controllable and predictable aerodynamic flowfield, contrary to using a commercial off the shelf (COTS) rotor. Due to complex aeroacoustic phenomena seen in an anechoic chamber testing campaign, three run conditions were selected to further investigate noise generating mechanisms specific to each case.

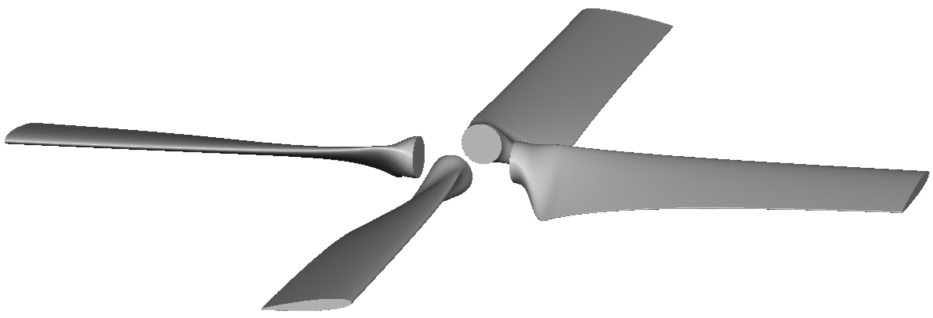

Fig. 1 Rotor geometry.

Aerodynamic loading results and acoustic measurements were available from a test campaign in the Small Hover Anechoic Chamber (SHAC) facility at the NASA Langley Research Center [12]. These experimental results were used for comparison to the multifidelity predictions performed throughout the scope of this work and will be discussed in

Section III.

Based upon data acquired from Ref. [12], the nominal condition, for which the ideally twisted rotor was designed to induce uniform inflow, produced 2.27 lb of thrust at ambient standard temperature and pressure (STP), and was selected as the first run condition. Cases with lower rotational rates showed pronounced energy content around 6 kHz, which was thought to be caused by laminar boundary layer vortex shedding (LBL-VS), or noise due to feedback mechanisms associated with naturally occurring instability waves in a transitional boundary layer [3]. Because of this, a second, off design run condition was selected to be $\Omega = 2929$ RPM, for which the rotor produced 0.587 lb of thrust. It was also seen that decreasing the collective blade pitch, θ_0, from its nominal value ($\theta_t = 6.9°$) to approximately $\theta_0 = -3°$ ($\theta_t = 4°$) mitigated the spectral peak around 40 kHz; however, with the addition of peculiar frequency content around 18 kHz, which was thought to be attributed to transitional boundary layer behavior. The third and final run condition, which was also off design, was chosen to be $\Omega = 5500$ RPM with a collective pitch of $\theta_0 = -2.7°$ ($\theta_t = 4.2°$), which produced 1.45 lb of thrust. The three run conditions are tabulated in Table 1 for clarity.

Table 1 Run conditions.

Case	Rotation Rate (Ω)	Collective Pitch (θ_0)	Blade Tip Pitch (θ_t)	Tip Mach Number (M_t)
Nominal	5500 RPM	$\theta_0 = 0°$	$\theta_t = 6.9°$	0.269
Low RPM	2929 RPM	$\theta_0 = 0°$	$\theta_t = 6.9°$	0.143
Low Collective	5500 RPM	$\theta_0 = -2.7°$	$\theta_t = 4.2°$	0.269

First, a preliminary simulation was conducted to predict the flowfield surrounding the rotor at the nominal, or design condition, using a lattice-Boltzmann method–very-large-eddy simulation (LBM-VLES) solver, PowerFLOW. One-third octave band sound pressure level ($SPL_{1/3}$) values of the unsteady, surface pressure perturbations were calculated, similar to what was done in Refs. [2, 11], to show regions of particular importance to broadband noise, which will be discussed in Section III.A. These $SPL_{1/3}$ contours were then used to split each blade into separate regions, which were thought to exhibit flow physics associated with different broadband noise mechanisms. Simulations with a finer spatial resolution at the three run conditions were then conducted using PowerFLOW. The split blade regions were each treated as individual, impermeable Ffowcs Williams and Hawkings (FW-H) surfaces, which were then provided to an implementation of Farassat's formulation 1A [14] that calculated acoustic pressure time history from each FW-H surface at defined observer locations. This was done within the post-processing software suite, PowerACOUSTICS. This allowed for the extraction of acoustic contributions from individual broadband noise mechanisms acting on different parts of the blade, namely, inboard separation noise, tip vortex formation noise, and leading edge noise.

Broadband noise predictions were also conducted using the ANOPP2 Broadband Acoustic Rotor Tool (ABART) [15], which entails the semiempirical method of Brooks, et al. [3]. Aerodynamic quantities pertinent to these ABART predictions as well as tonal acoustic noise predictions were generated using the ANOPP Propeller Analysis System (PAS) [16]. This method will hereafter be referred to as PAS-ABART.

Physical insight was gained from the PowerFLOW simulations in this work, and ABART boundary layer trip settings along with LBL-VS settings were modified from the standard approach previously used in Refs. [1, 6] to account for aerodynamic phenomena such as tip vortex formation and boundary layer transition along the span of the rotor blade.

A. Lattice-Boltzmann Methodology

The lattice-Boltzmann method (LBM) employed by the commercial software suite, PowerFLOW, was used throughout this work due to its proven accuracy on similarly complex rotorcraft problems [2, 9–11]. LBM is based on kinetic theory and uses a statistical description of discrete particle motion along 19 directions in three-dimensional space (D3Q19). LBM is explicit in nature, solving first for the convection of mesoscopic fluid particles before solving for the collision of these particles using the Bhatnagar-Gross-Krook model [17]. The reader is referred to Refs. [18, 19] for a more detailed theoretical explanation of LBM.

Contrary to standard turbulence modeling procedures used by traditional Navier-Stokes solvers, which use closure models to approximate the Reynolds stress as an effective eddy viscosity contribution to the governing equations, PowerFLOW uses a very-large-eddy simulation (VLES) to calculate a turbulent relaxation time based upon local turbulence parameters: strain, vorticity, and helicity [9]. The method for calculating this relaxation time is similar to that of traditional two-equation turbulence closure models, but it is used to recalibrate the viscous relaxation time in the Boltzmann equation to the relevant time scales associated with turbulent motion. In this fashion, the unresolved,

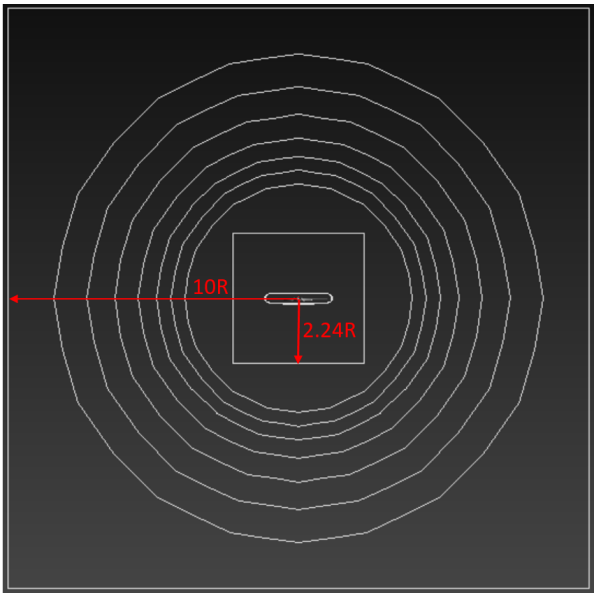

Fig. 2 Full computational domain visualization.

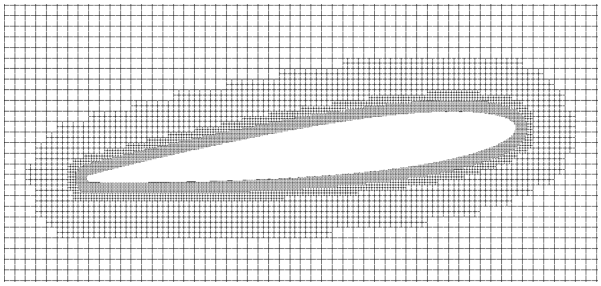

Fig. 3 Nearfield resolution visualization along rotor blade.

subgrid turbulence is realized by the governing equation.

In addition to modeling the subgrid turbulence, PowerFLOW uses a geometry cut-cell approach in conjunction with wall functions, which are extended to include the effects of pressure gradients, to generalize the near wall turbulence to that of the well known universal turbulence profile, the Law of the Wall [20]. This technique significantly reduces the computational cell count by eliminating the need for body fitted, stretched boundary layer grids like those commonly associated with traditional Navier-Stokes solvers.

B. Computational Setup

The computational domain was discretized automatically within the PowerFLOW suite using purely hexahedron cells, or voxels, in a similar fashion as in Ref. [2], which can be seen in Fig. 2. The extents of this computational domain and its constituents are such that the cylindrical region encompassing the rotor and nearfield spanned 2.24R away from the rotor in all directions, whereas the farfield, cuboidal region was 10R away from the rotor.

Three finely resolved regions directly offsetting the rotor were defined and are shown for a fine resolution case in Fig. 3 for clarity. The resolution of the finest voxel, adjacent to the rotor geometry is shown in Table 2 in inches as well as on a rotor chord percentage basis for both the preliminary simulation and for the three final simulations. Each successive region moving outward from the rotor doubled the cell size of the former region, as seen in Fig. 3. A series of spheres were defined, growing outward from the near wake cylindrical region to gradually decrease the spatial resolution until the farfield, cuboidal boundary.

Table 2 Finest voxel size.

Case	Finest Voxel Size (inches)	Finest Voxel Size (%c)
Coarse Resolution	0.003125	0.250
Fine Resolution	0.001923	0.154

The total voxel count, fine equivalent voxel count, time step, and computational cost for each of the simulations are shown in Table 3. The time step was internally calculated by PowerFLOW using a Courant-Friedrichs-Lewy (CFL) number of 1 and given the aforementioned simulation parameters of the finest voxel size. A CFL number of 1 was maintained for the temporal update of each voxel throughout the computational domain, meaning that a voxel in a given resolution region updated half as often as a voxel in an adjacent region of finer resolution, defining the 'fine equivalent' voxel metric.

Table 3 Simulation properties.

Case	Total Voxel Count	Fine Equivalent Voxel Count	Time Step	CPU Hours
Coarse Resolution	302 million	98 million	1.195E-07 sec	3.5E+03 hours
Fine Resolution	1.2 billion	382 million	7.357E-08 sec	8.2E+05 hours

A no-slip boundary condition was imposed on the rotor surface and ambient STP conditions, as well as a zero velocity condition, were imposed on the outer boundaries of the computational domain for these hover cases. Transitional wall functions were used in the first voxel adjacent to the rotor geometry to approximate the boundary layer up to the y+ distances shown in Table 4.

Table 4 y+ distances at various spanwise locations.

	y+ Distances		
Case	0.25R	0.5R	0.75R
Preliminary (5500 RPM)	6.54	12.45	18.14
Final (5500 RPM)	4.03	7.66	11.17
Final (2929 RPM)	2.24	4.27	6.22

C. Acoustic Data Post-Processing

All PowerFLOW simulations for both the preliminary case as well as for the final cases were conducted over 14 rotor revolutions, with the last 6 being used to record unsteady surface pressures on the rotor at a sampling rate of 133 kHz. Convergence of the aerodynamic flowfield surrounding the rotor had been determined to occur at the 8th revolution.

Techniques similar to those of Refs. [1] and [2] were used to post-process the acoustic pressure time histories from both the simulation and the experiment to differentiate between the periodic (tonal) and stochastic (broadband) noise contributions of each data set. This subsection discusses how the signal differentiation process was applied to the computational data sets. The reader is referred to Ref. [12] for specific processing details pertaining to the experimental data.

First, the acoustic pressure time history was separated into six equally sized bins correspondent to the six rotor revolutions of recorded data. These six revolutions were averaged together to obtain a mean rotor revolution, which served as the basis for the subsequent tonal noise calculations. This mean rotor revolution was then subtracted from each of the six bins of raw acoustic pressure time history data to obtain the residual acoustic pressure time history, or broadband noise component.

The residual (broadband) acoustic pressure time history was treated as an aperiodic signal of which the Fast Fourier Transform was calculated. The SPL and power spectral density (PSD) of these processed signals were then calculated using Equations 1 and 2, the former of which used a frequency resolution of 50 Hz due to the limited number of rotor revolutions of data. The SPL data were then used to calculate $SPL_{1/3}$ values. These post-processing techniques were used on the acoustic pressures propagated to an out-of-plane observer location, which was 35 degrees below the rotor plane at a radial distance of 11.94R away.

$$\mathrm{SPL} = 10\log_{10}\left(\frac{P_{xx} * \Delta\mathrm{f}}{p_{\mathrm{ref}}^2}\right) \tag{1}$$

$$\mathrm{PSD} = 10\log_{10}\left(\frac{P_{xx}}{p_{\mathrm{ref}}^2}\right) \tag{2}$$

Another post-processing technique was used for calculating directivity trends that filtered the mean (tonal) acoustic pressure time history using a second-order Butterworth narrow bandpass filter with a ±30 Hz frequency band centered at the first two blade passage frequency (BPF) harmonics. This filter served the purpose of mitigating spectral leakage associated with different measurement and post-processing techniques. This effectively confined all energy associated with each BPF harmonic to the frequency value of the harmonic itself, allowing for a better comparison between the

spectral data of the simulation and that of the experiment. The root mean square (RMS) value of this filtered data was used to calculate the SPL amplitudes of each BPF harmonic using Equation 3.

$$\mathrm{SPL}_{n*BPF} = 20\log_{10}\left(\frac{\bar{p}_{\mathrm{rms}}}{p_{\mathrm{ref}}}\right) \tag{3}$$

III. Results

A. Coarse PowerFLOW Simulation Results

The thrust calculated from the preliminary simulation was seen to be 1.94 lb, which was underpredicted from the experimental results by 14.54%. This run condition was used primarily for the identification of regions along the rotor blades of particular aeroacoustic interest. This was done by calculating the $SPL_{1/3}$ values of the surface pressure perturbations, which can be seen in Fig. 4 at one-third octave band center frequencies between 1 kHz and 10 kHz on the suction and pressure sides of a rotor blade, respectively. It should be noted that these pressure perturbations are in source time and are technically not acoustic pressures. However, since they are the pressure residuals, they are believed to be indicative of broadband noise generation in source time.

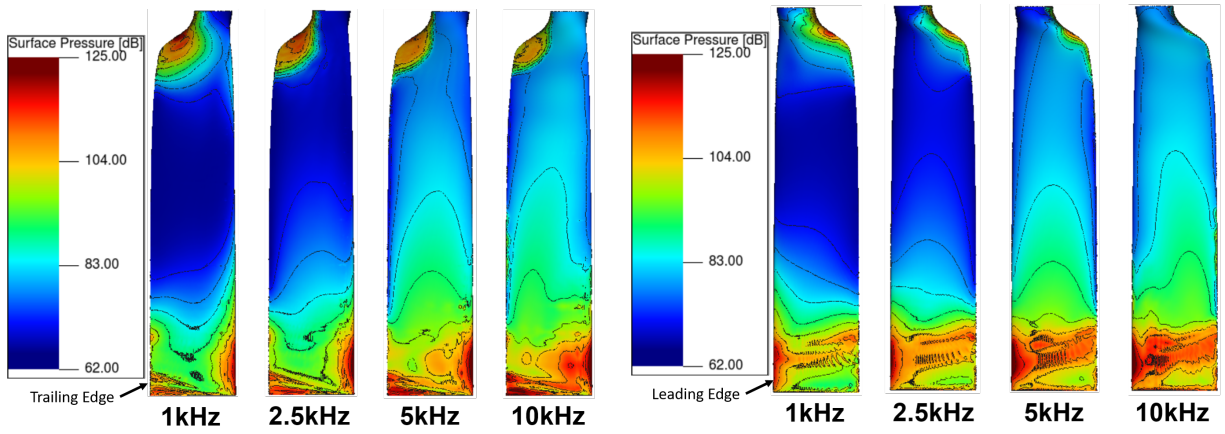

(a) Suction side. **(b) Pressure side.**

Fig. 4 $SPL_{1/3}$ contours of surface pressure perturbations. Range: 62 dB - 125 dB.

As it can be seen in Fig. 4, there are prominent surface pressure fluctuations at the inboard region of the blades at lower frequencies. Since the flow velocity is close to zero at the blade root and because the blade root is cylindrical in shape with an abrupt transition to the blade profile, this region of intense pressure perturbations is caused by local flow separation. It can also be seen that leading edge noise is prominent throughout the frequency range depicted. Since the rotor consists of 4 blades, the tip vortices being generated have little time to convect downward before they reach the following blade, having a miss distance between the center of the viscous core and the blade's leading edge of $\Delta = 0.275c$. The small miss distance suggests that the leading edge noise is caused by blade wake interaction (BWI), or perpendicular blade vortex interactions [8]. The ripple-like behavior on the pressure side of the blades is also attributed to the wake entrained by this perpendicular vortex passing by the blade. Lastly, it can be seen at the blade tips, from approximately half of the blade chord to the trailing edge, that as the tip vortex is being formed by spilling over from the pressure side of the blade to the suction side, high levels of pressure perturbations are being induced. This mechanism is more prominent at the higher frequencies and is shown in Fig. 5 at 10 kHz for clarity.

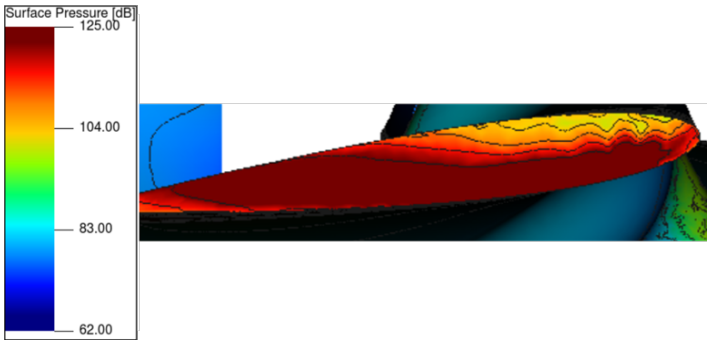

Fig. 5 $SPL_{1/3}$ of surface pressure perturbations looking inboard from the tip (10 kHz). Range: 62 dB - 125 dB.

Based on these observations, the blade surface was partitioned into five regions of interest as shown in Fig. 6. The region furthest inboard on the blade, Region I, spanned from the root to 0.2614R, slightly past the region of intense pressure perturbations caused by local flow separation. The second region, Region II, spanned the blade from 0.2614R to 0.8154R, which was done to separate the noise from the midspan of the blade to further isolate the inboard and outboard regions. Starting from 0.8154R to the blade tip, the leading edge of the blade to 0.25c on both the surface and suction sides was treated as a separate surface, Region IV, to capture the leading edge noise caused by BWI and TIN. The outboard, 0.1846R of the blade from 0.25c to the trailing edge was split into two sections, Region III and Region V. The outermost section, Region V, was split at 0.9795R and was created to isolate the tip vortex formation noise from the blade self-noise generated by pressure scattering of the near wake turbulence on the trailing edge [3]. Region V also included the end cap of the blade. These regions were each treated as separate FW-H surfaces to differentiate between noise mechanisms from the different areas along the blade. They will herein be referred to by their region numbers as discussed in this section and as shown in Fig. 6.

Fig. 6 Rotor blade split into separate FW-H surfaces (top view).

B. Fine PowerFLOW Simulation Aerodynamic Results

Integrated thrust results for the final PowerFLOW simulations are provided in Table 5 and compared to the experimentally measured values. It can be seen in Table 5 that the thrust for the nominal PowerFLOW case is underpredicted compared to the experimental value by 9.25%, a 5.3% improvement from the preliminary simulation. A similar trend was seen in Ref. [2] during a grid sensitivity study for very similar spatial resolutions. It was shown in Ref. [2] that this underprediction in thrust may be attributed to an overprediction of induced velocity.

Table 5 Predicted thrust results.

Case	Experimental	PowerFLOW	
		Thrust	Relative Error
Nominal (5500 RPM)	2.27 lb	2.06 lb	9.25%
Low RPM (2929 RPM)	0.587 lb	0.554 lb	5.62%
Low Collective (5500 RPM)	1.45 lb	1.25 lb	13.8%

C. Fine PowerFLOW Simulation Aeroacoustic Results

1. Tonal Noise Comparison

Directivity plots of the fundamental and second BPF harmonic along a radial arc located 11.94R away from the rotor were generated using the BPF filtering technique discussed in Section II.C and are plotted in Figs. 7 and 8 against experimentally acquired results as well as against results generated using PAS for all three run conditions. The PAS predictions for the fundamental BPF shown in Fig. 7 are seen to be within 4 dB of the experimental data. The PowerFLOW simulations, however, are seen to underpredict by approximately 7 dB except for at the -35 degree observer location for the low RPM case. This can be attributed to the underprediction in thrust from the simulations.

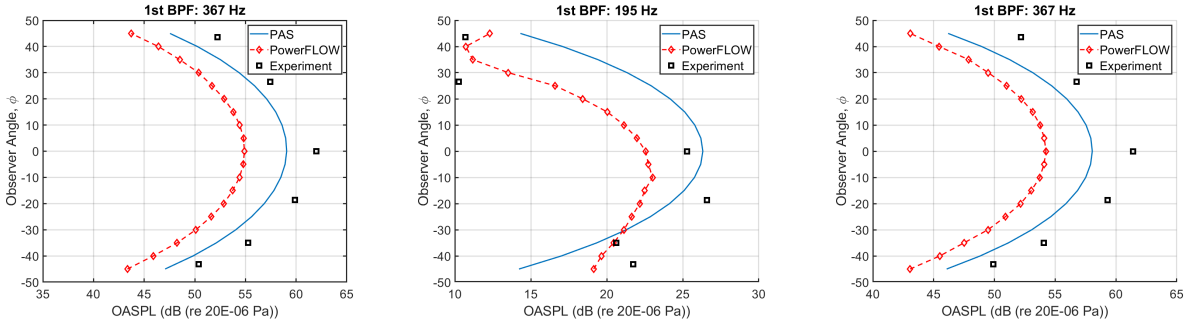

(a) Nominal case. **(b) Low RPM case.** **(c) Low collective case.**

Fig. 7 Directivity plots of fundamental BPF at 11.94R.

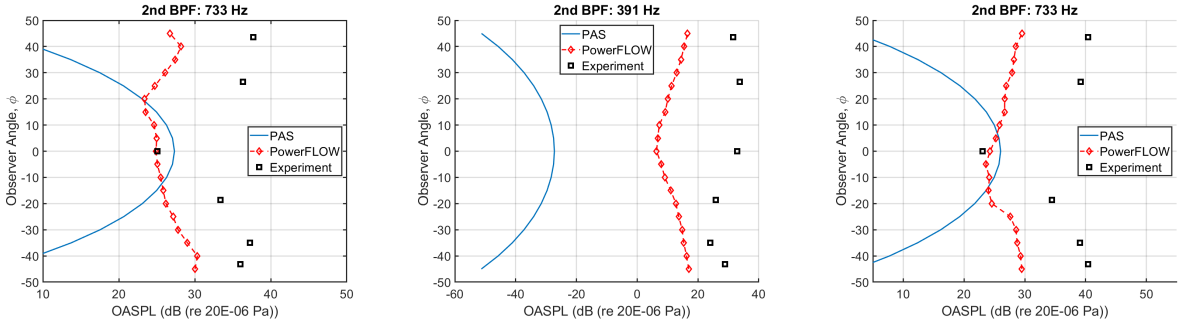

(a) Nominal case. **(b) Low RPM case.** **(c) Low collective case.**

Fig. 8 Directivity plots of second BPF at 11.94R.

The second harmonics of the BPF in Fig. 8 are predicted within 1 dB by PowerFLOW at the in-plane observer location for the nominal and low collective cases. The general trend in directivity of the second BPF harmonic is also reasonably approximated by the PowerFLOW simulations for the nominal and low collective cases at all other observer locations; however, the amplitudes are underpredicted by similar values as in Fig. 7. The PowerFLOW simulation did not capture the second harmonic of the BPF directivity trend observed in the experiment for the low RPM case; however, the amplitudes have less of an underprediction at observers located below the plane of the rotor when compared to the other two cases. The general directivity trend of this second harmonic is completely missed by PAS, similar to Refs. [1, 2].

2. Broadband Noise Comparison

Broadband noise behaves as a dipole noise source in the context of an impermeable FW-H implementation, so an out-of-plane observer location was selected to evaluate this type of noise. Plots for the acoustic PSD and $SPL_{1/3}$ at the out-of-plane observer located 35 degrees below the rotor plane have been generated for all three run conditions and are compared against the experimental results in Figs. 9 and 10. These plots show a slight overprediction by PowerFLOW for the nominal and low collective cases, but good overall agreement between the predictions and experimental results

in the range of 1 kHz - 20 kHz for all three cases, followed by a gradual roll off in the spectra. It is thought that the predictions lack the capability of matching results at these higher frequencies due to the spatial resolution used.

The previously mentioned tonal behavior around 18 kHz for the low collective case was also accurately predicted, as seen in Figs. 9c and 10c. Figure 9 shows that there are discrete tones occurring at approximate harmonics of the BPF between 2 kHz and 12.5 kHz for both the predictions as well as the experimental data for the nominal and low collective cases and between 800 Hz and 5 kHz for the low RPM case, which exhibits behavior matching that of TIN [21, 22]. It is believed that the eddies associated with this TIN noise were induced by a BWI event, which will be discussed in subsequent sections. Although the low collective case may have had a smaller vortex miss distance than the nominal case, it appears as though the BWI event may be stronger for the nominal case, denoted by the larger tonal amplitudes between 2 kHz and 12.5 kHz in Fig. 9a. It should be noted here that the experimental rotational rates were close to the simulated values; however, rates differed by as much as 141 RPM from the simulations. Because of this, the experimental frequencies in Fig. 9 were scaled to match those of the simulations.

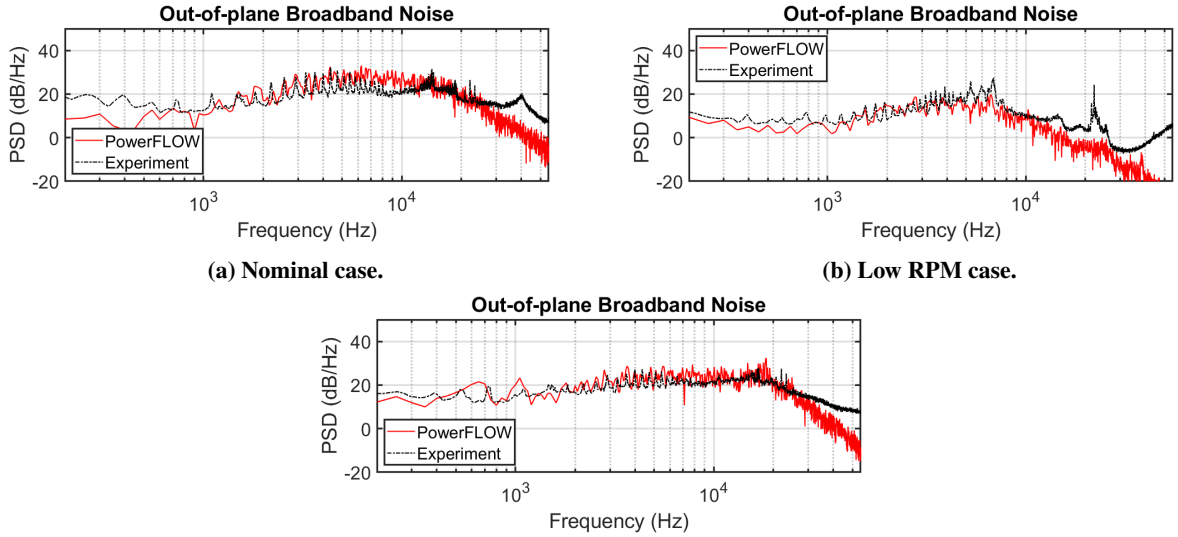

(a) Nominal case.

(b) Low RPM case.

(c) Low collective case.

Fig. 9 Broadband noise narrowband autospectra at $\phi = -35°$.

The broadband noise was filtered using the same technique mentioned in Section II.C; however, overall sound pressure level (OASPL) values were calculated over the range of 500 Hz to 10 kHz. The predicted results for all three run conditions have been plotted in Fig. 11 against experimentally acquired data and against predictions performed using PAS-ABART. The PAS predictions used a uniform flow assumption, which does not take the tip vortex formation into account. It is known for rotorcraft that there is an effective blade area responsible for thrust generation correspondent to approximately 95% - 98% of the original blade span due to the tip vortex [13]. To account for the effect of this tip vortex on the suction side boundary layer, the ABART predictions were conducted with the boundary layer being tripped for the last 5% of the blade span, with the inboard 95% being untripped. The broadband noise directivities are seen to match well between the PowerFLOW simulations and the experimental results for the nominal and low collective cases, with an underprediction at the in-plane observer location. The low RPM case was underpredicted by approximately 7 dB at all observer locations with an increased underprediction at the in-plane observer location. Since the broadband noise behaves as a dipole, this in-plane observer location exhibits a null region, and it is thought that this observer location is less representative of the overall trend in broadband noise when compared to other observer locations. The PAS-ABART predictions are seen to underpredict by approximately 6 dB at most observer locations, further illustrating the inability of this method to predict noise sources caused by complex, 3D rotorcraft aerodynamics, namely, BWI and TIN. Note that the PAS-ABART predictions did not include LBL-VS for the directivity plots shown in Fig. 11.

3. Aeroacoustic Noise Sources

In an effort to characterize the effects of BWI and TIN, the acoustic contribution from all of the previously defined blade regions, with the exception of the leading edge region, Region IV, has been plotted against the total predicted

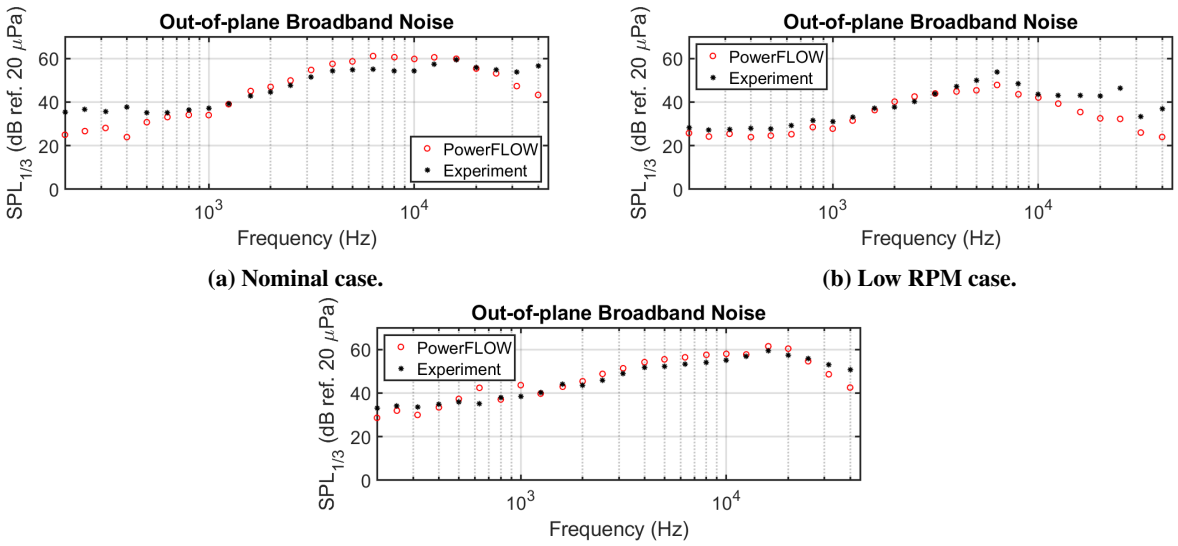

(a) Nominal case.

(b) Low RPM case.

(c) Low collective case.

Fig. 10 Broadband noise one-third octave spectra at $\phi = -35°$.

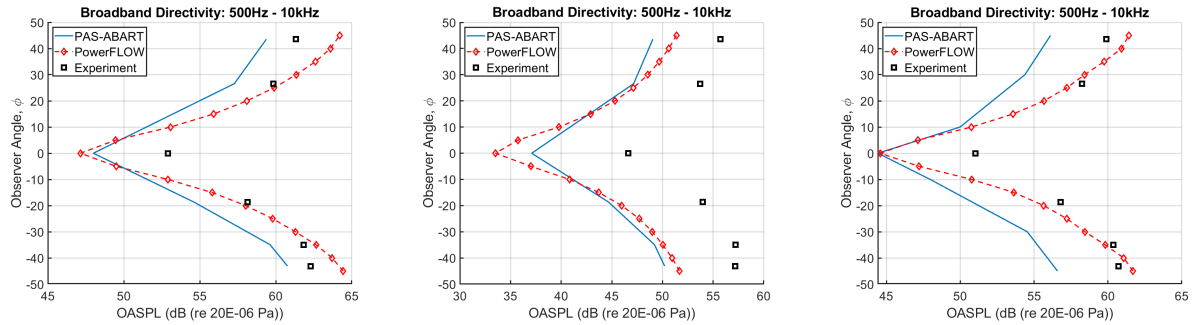

(a) Nominal case.

(b) Low RPM case.

(c) Low collective case.

Fig. 11 Broadband noise directivity at 11.94R.

results and the experimentally acquired results at the out-of-plane observer location on an $SPL_{1/3}$ basis in Fig. 12.

Figure 12 shows that the leading edge noise from Region IV and hence the BWI noise and TIN are responsible for an increase of approximately 6 dB between 2 kHz and 12.5 kHz for the nominal and low collective cases and between 800 Hz and 5 kHz for the low RPM case. All three run conditions had very similar BWI noise and TIN contributions with the low RPM case being shifted to a lower frequency range, signifying that these noise sources may not be dependent on vortex miss distance. For reference, the vortex miss distances have been tabulated for all three run conditions in Table 6.

Table 6 Vortex miss distances.

Case	Vortex Miss Distance (Δ/c)
Nominal Case	0.2745
Low RPM Case	0.2898
Low Collective Case	0.1545

BWI is a quasisteady phenomenon since each tip vortex will hold the same miss distance away from a subsequent blade for a given run condition. This should be indicative of an overall increase in the broadband noise; however, Fig. 9 illustrates that the increase in broadband noise caused by the leading edge shown in Fig. 12 is caused by discrete tonal behavior occurring at BPF harmonics, which is characteristic of TIN noise. It is believed that the entrained blade wake in the tip vortex system is responsible for this leading edge noise. These tip vortices are constantly spinning, regardless of their proximity to subsequent blades, so this entrained turbulence is spinning as well, behaving in an unsteady fashion. The induction of this unsteady, entrained turbulence into the rotor system by the tip vortices as they impinge on the leading edge of subsequent blades is

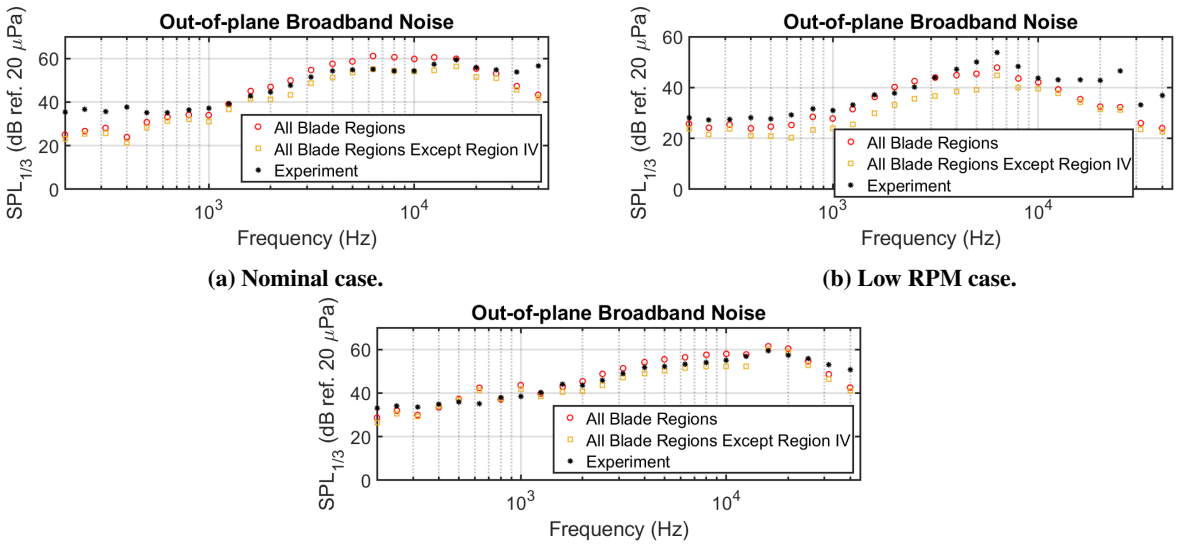

(a) Nominal case.

(b) Low RPM case.

(c) Low collective case.

Fig. 12 Broadband noise one-third octave spectra without leading edge at $\phi = -35°$.

thought to be the culprit of this TIN-like behavior.

By excluding Region IV from the spectra, not only have the effects of BWI and TIN been identified, but the broadband self-noise has also been isolated. The self-noise emanating from different portions of the blade is shown in Fig. 13 by plotting the acoustic accumulation of all blade regions except for Region IV, as well as individual contributions of these regions. Figure 13 shows that the inboard section of the blade, Region I, has a negligible contribution to the overall spectra meaning that the local flow separation caused by the cylindrical portion of the blades has little to no acoustic impact. This can be explained by the low velocities at the inboard region of the rotor. It can also be seen that the tip vortex formation noise from Region V only has an impact at frequencies above 30 kHz for both the nominal case and the low collective case. This frequency is shifted to 16 kHz for the low RPM case.

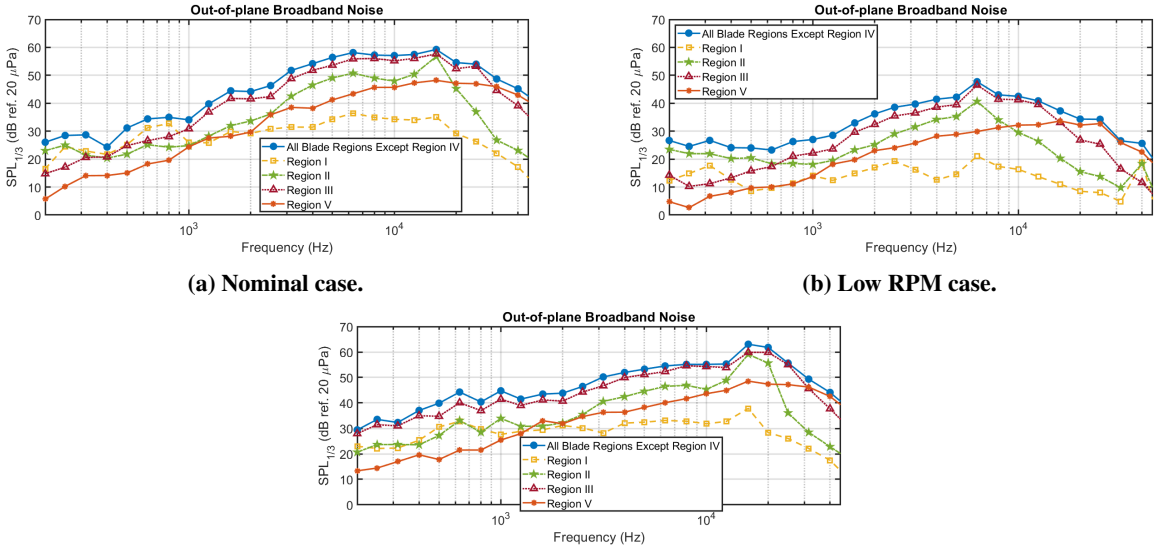

(a) Nominal case.

(b) Low RPM case.

(c) Low collective case.

Fig. 13 Broadband self-noise one-third octave spectra at $\phi = -35°$.

Region III produces almost all of the generated self-noise, which was somewhat expected, based upon the results

shown in Fig. 4. Interestingly, the tonal behavior located at the 16 kHz one-third octave band for the nominal and low collective cases appears in the spectra at the same magnitude for both Region II and Region III. This same tonal behavior occurs at 6.3 kHz for the low RPM case and Region II exhibits a much lower amplitude than Region III. Skin friction values along the chord were taken just inboard of Region III at 81% of the blade span to determine the cause of this noise as it appears in Region II. Figure 14 shows that the pressure side of the blade is transitioning to turbulence, denoted by the abrupt increase in skin friction. This figure also shows that the turbulent region of the boundary layer is much smaller for the low RPM case, explaining why this tonal behavior at 6.3 kHz from Region II has a smaller amplitude than for the other two cases. Since both the pressure side and the suction side of the blade are turbulent, there is a much larger boundary layer displacement thickness, δ^*, and thus a larger effective blade thickness. This, coupled with the pressure difference between the pressure and suction sides of the blade and the fact that the trailing edge is rounded, is believed to produce a form of quasisteady vortex shedding, commonly associated with bluff bodies. This vortex shedding behavior is thought to be characteristic of the broadband self-noise mechanism, LBL-VS, which is traditionally caused by natural transition to turbulence.

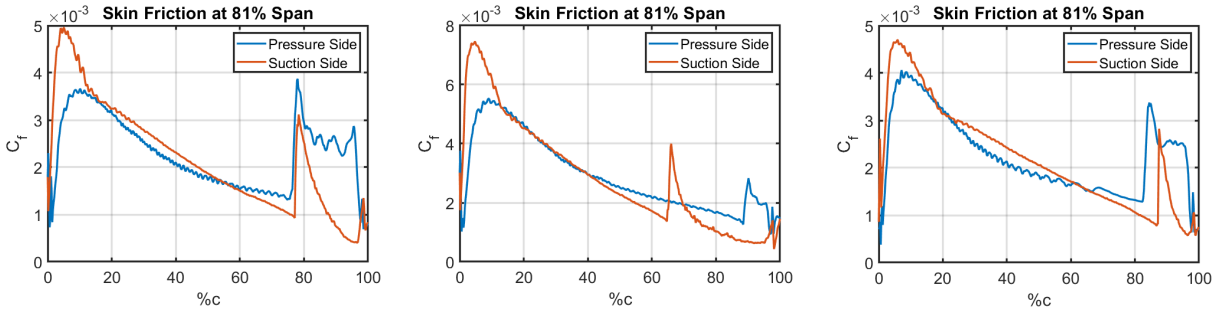

(a) Nominal case. **(b) Low RPM case.** **(c) Low collective case.**

Fig. 14 Nondimensional skin friction at 81% span.

This is validated in Fig. 15 by comparing the PowerFLOW predictions for all blade regions except Region IV against predictions conducted using PAS-ABART with the inclusion of LBL-VS. This was done to obtain a one-to-one comparison between the semiempirical self-noise prediction method and the isolated self-noise predicted by PowerFLOW. These PAS-ABART predictions maintained a tripped boundary layer over the last 5% of the blade span, as previously discussed; however, since the LBL-VS behavior was shown to appear around approximately 80% of the span, a Reynolds number limit of 16E+04 was imposed on the LBL-VS so that it would only be calculated over approximately 80% of the blade span for the nominal case and over the entirety of the blade for the low RPM case. Reasonable agreement can be seen for frequencies above 1 kHz, with an overprediction from PAS-ABART in the region of LBL-VS noise. It is interesting to note the similar frequency and magnitude of the LBL-VS noise from PowerFLOW and PAS-ABART for both the nominal case and the low RPM case. It was seen that this LBL-VS noise was drastically overpredicted by PAS-ABART for the low collective case when using the 16E+04 Reynolds number limit, so the limit for this case was reduced to 13.5E+04, which reduced the region over which LBL-VS was calculated to approximately 65% of the blade span. It was assumed that the transitional behavior responsible for LBL-VS noise is occurring further inboard due to the smaller vortex miss distance and the closer proximity of the blade wake to subsequent blades as shown in Fig. 16c. Although the amplitude of this LBL-VS noise for the low collective case is predicted accurately, the reduction of the Reynolds number limit shifted the frequency at which this noise occurs from 16 kHz to 8 kHz.

It was necessary to determine the cause of transition on the pressure side boundary layer since this is not a common occurrence. Nondimensional vorticity plots have been generated along the half chord for all three cases in Fig. 16 with the 81% spanwise location denoted by the green/red line. It is evident from this figure that the complex vortex system is responsible for the pressure side transition at the 81% spanwise location. As the tip vortex from the preceeding blade traverses along the chord of the following blade, it induces turbulence into the rotor system, as previously discussed. Not only does this vortex cause local downwelling on the pressure side boundary layer, but the entrained turbulence is further induced by the tip vortex from the second preceeding blade in the region of this transitional behavior, indicating that the presence of this vorticity field has a destabilizing effect on the boundary layer, forcing it to transition from laminar to turbulent.

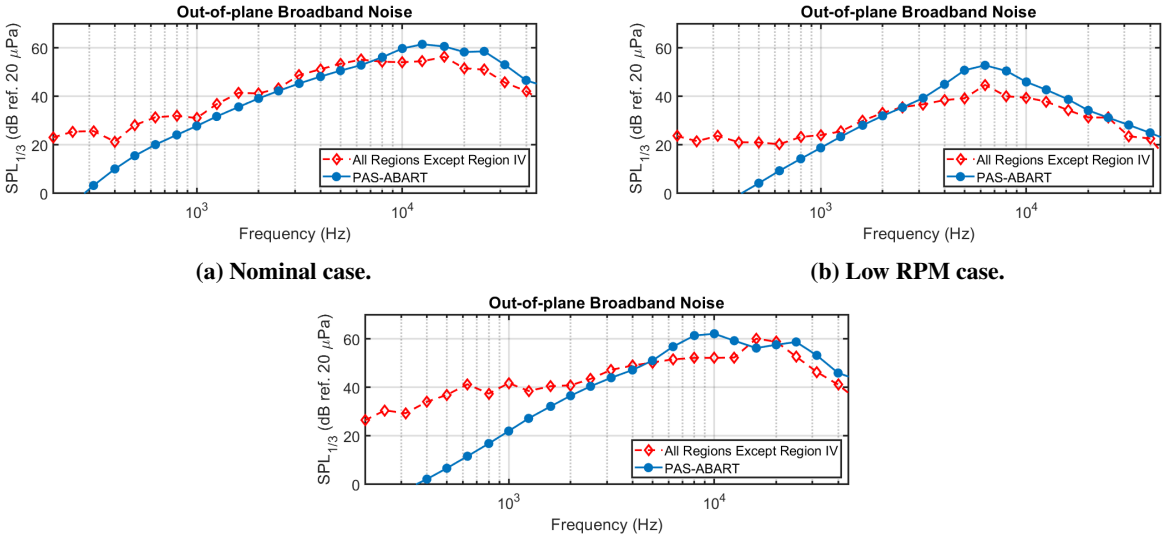

(a) Nominal case.

(b) Low RPM case.

(c) Low collective case.

Fig. 15 Broadband self-noise one-third octave spectra at $\phi = -35°$.

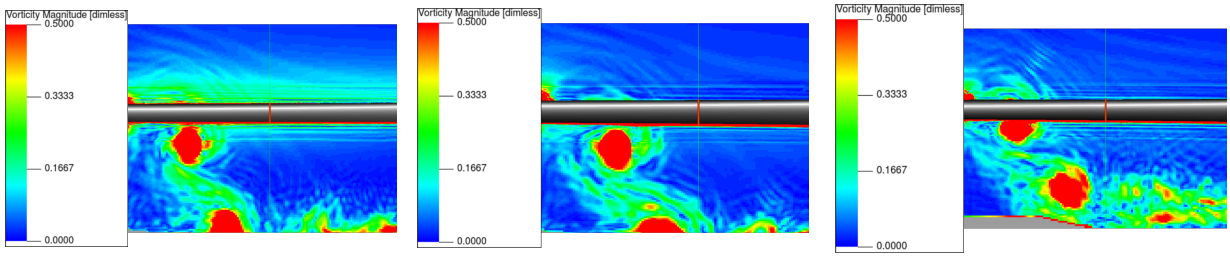

(a) Nominal case.

(b) Low RPM case.

(c) Low collective case.

Fig. 16 Nondimensional vorticity.

IV. Conclusions and Future Work

This work evaluated the use of LBM-VLES for aeroacoustic simulations of an ideally twisted rotor with a focus on identifying broadband noise sources. A preliminary simulation of the nominal case was first conducted at a coarse spatial resolution to determine blade regions of particular importance to broadband noise by calculating $SPL_{1/3}$ values of the unsteady surface pressures. These $SPL_{1/3}$ contours were then used to identify five different regions thought to be responsible for different broadband noise mechanisms such as tip vortex formation noise, inboard separation noise, and leading edge noise. Using this split geometry, finely resolved simulations were conducted for the three run conditions and each of the different blade regions were treated as separate impermeable FW-H surfaces. These surfaces were then provided to the post-processing software suite, PowerACOUSTICS, which calculated acoustic pressure time histories at prescribed observer locations using an implementation of Farassat's formulation 1A [14]. Thrust predictions from the three simulations were compared to experimentally acquired data with relative error values that were less than 10% for the nominal and low RPM cases and less than 15% for the low collective case.

Acoustic data were post-processed and directivity of the fundamental and second BPF harmonics along a radial arc located 11.94R away from the rotor were compared against experimentally acquired data as well as against predictions conducted using ANOPP's PAS. These comparisons showed larger underpredictions from the PowerFLOW simulations than from the PAS simulations for the fundamental BPF. It was also shown that overall trends from the PowerFLOW simulation were representative of the experimental results for the second BPF harmonic directivities with underpredicted amplitudes, and the PAS simulation failed to capture this trend for the second BPF harmonic. Broadband $SPL_{1/3}$ narrowband spectra showed excellent agreement between the broadband noise predicted using PowerFLOW and the experimentally acquired data. Broadband PSD results also illustrated that there was discrete tonal behavior occurring at

BPF harmonics between 2 kHz and 12.5 kHz for the nominal and low collective cases and between 800 Hz and 5 kHz for the low RPM case. Results generated from the accumulation of all split regions of the rotor except for the leading edge further proved that this discrete tonal behavior was responsible for approximately a 6 dB increase in broadband noise for all three run conditions, showing that this leading edge noise has negligible dependence on vortex miss distance. Since this leading edge noise exhibited tonal behavior commonly associated with TIN, it was thought that the tip vortices from preceeding blades were inducing turbulence associated with blade wake. This induced turbulence then impinged on the leading edge of following blades in an unsteady fashion resulting in TIN-like behavior being caused by a BWI event.

By removing the acoustic contribution from the leading edge section, the broadband self-noise was isolated and studied in more detail to show that inboard separation noise had a negligible contribution and that the tip vortex formation noise only appeared at frequencies above 30 kHz for the nominal and low collective cases and at frequencies above 16 kHz for the low RPM case. It was also seen that the pronounced tonal behavior at 16 kHz for the nominal and low collective cases and at 6.3 kHz for the low RPM case originated from the middle section of the blade, Region II, and Region III, which encompassed the downstream 0.75c of the blade between 81.54% and 97.85% span. Skin friction values at the 81% spanwise location indicated that the pressure side boundary layer was transitioning to turbulence, which was shown to be caused by downwelling and destabilization of the boundary layer by the turbulence field induced by tip vortices as they traversed subsequent blades. It is believed that since both the pressure and suction sides of the rotor blades are turbulent, there is a larger effective boundary layer displacement thickness, δ^*, and thus a larger effective blade thickness, which produces a form of quasisteady vortex shedding past the rounded trailing edge. This vortex shedding behavior is thought to be characteristic of the broadband self-noise mechanism, LBL-VS, which was further validated by comparing the isolated self-noise PowerFLOW predictions to PAS-ABART predictions conducted with the boundary layer of the last 5% of the blade span being tripped. The PAS-ABART predictions also included the calculation of LBL-VS over the blade span up to approximately 80% for the nominal case, 100% for the low RPM case, and 65% for the low collective case.

It is apparent from this work that further research is needed to characterize BWI noise and TIN for rotors in hover. It should be noted that these types of noise will be negligible for other flight conditions such as forward flight since the wake will be convected away from the rotor. Although these broadband noise mechanisms contributed 6 dB for this specific rotor, it is believed that there will be a much more drastic effect for larger rotors, and the current low-fidelity methods lack the ability to capture these types of noise. It is anticipated that future work will look at characterizing BWI noise and TIN in hopes of creating low-fidelity prediction models to be used in conjunction with the methodology of Brooks, et al. [3] to obtain more accurate broadband noise predictions without the need for costly, high-fidelity flow simulations. With the addition of these two noise sources in the overall broadband noise calculation, more accurate optimization procedures may be implemented to reduce the overall noise emanating from these sUAS and, ultimately, larger urban air mobility vehicles.

Acknowledgments

The authors would like to thank David Lockard of the Computational Aerosciences Branch at NASA Langley Research Center for his assistance in allocating computational resources, which were vital to this research. This work was funded by the NASA Revolutionary Vertical Lift Technology (RVLT) project.

References

[1] Zawodny, N. S., Boyd Jr., D. D., and Burley, C. L., "Acoustic Characterization and Prediction of Representative, Small-Scale Rotary-Wing Unmanned Aircraft System Components," *AHS International 72nd Annual Forum*, West Palm Beach, FL, May 2016.

[2] Thurman, C. S., Zawodny, N. S., and Baeder, J. D., "Computational Prediction of Broadband Noise from a Representative Small Unmanned Aerial System Rotor," *VFS International 76th Annual Forum & Technology Display*, Virginia Beach, VA, October 2020.

[3] Brooks, T. F., Pope, D. S., and Marcolini, M. A., "Airfoil Self-Noise and Prediction," NASA RP 1218, 1989.

[4] Brooks, T. F., and Burley, C. L., "Blade Wake Interaction Noise for a Main Rotor," *Journal of the American Helicopter Society*, Vol. 49, No. 1, 2003, pp. 11–27.

[5] Brooks, T. F., and Burley, C. L., "Rotor Broadband Noise Prediction with Comparison to Model Data," *Journal of the American Helicopter Society*, Vol. 49, No. 1, 2001, pp. 28–42.

[6] Pettingill, N. A., and Zawodny, N. S., "Identification and Prediction of Broadband Noise for a Small Quadcopter," *VFS International 75th Annual Forum & Technology Display*, Philadelphia, PA, May 2019.

[7] Amiet, R. K., "Noise Produced by Turbulent Flow Into a Rotor: Theory Manual for Noise Calculation," NASA CR 181788, 1989.

[8] Wittmer, K. S., Devenport, W. J., and Glegg, S. A. L., "Effects of Perpendicular Blade-Vortex Interaction, Part 2: Parameter Study," *AIAA Journal*, Vol. 37, No. 7, 1999, pp. 813–817.

[9] Casalino, D., "Impingement of a Propeller-slipstream on a Leading Edge with a Flow-permeable Insert: A Computational Aeroacoustic Study," *International Journal of Aeroacoustics*, Vol. 17, 2018, pp. 5687–711.

[10] Gonzalez-Martino, I., Wang, J., Romani, G., and Casalino, D., "Rotor Noise Generation in a Turbulent Wake using Lattice-Boltzmann Methods," *24th AIAA/CEAS Aeroacoustics Conference*, Atlanta, GA, June 2018.

[11] Nardari, C., Casalino, D., Polidoro, F., Coralic, V., Brodie, J., and Lew, P., "Numerical and Experimental Investigation of Flow Confinement Effects in UAV Rotor Noise," *25th AIAA/CEAS Aeroacoustics Conference*, Delft, The Netherlands, May 2019.

[12] Pettingill, N. A., Zawodny, N. S., Thurman, C. S., and Lopes, L. V., "Acoustic and Performance Characteristics of an Ideally Twisted Rotor in Hover," *2021 SciTech Forum: AIAA Aeroacoustics Conference*, Nashville, TN, January 2021.

[13] Leishman, J. G., *Principles of Helicopter Aerodynamics*, Cambridge University Press, New York, NY, 2000.

[14] Farassat, F., "Derivation of Formulations 1 and 1A of Farassat," NASA TM 2007-214853, 2007.

[15] Lopes, L., and Burley, C., "ANOPP2 User's Manual: Version 1.2," NASA TM 2016-219342, 2016.

[16] Nguyen, L. C., and Kelly, J. J., "A Users Guide for the NASA ANOPP Propeller Analysis System," NASA CR 4768, 1997.

[17] Bhatnagar, P., Gross, E., and Krook, M., "A Model for Collision Processes in Gases. I. Small Amplitude Processes in Charged and Neutral One-Component Systems," *Phys. Rev.*, Vol. 94, 1954, pp. 511–525.

[18] Succi, S., *The Lattice Boltzmann Equation for Fluid Dynamics and Beyond*, 1st ed., Clarendon Press, Oxford, 2001.

[19] Shan, X., Yuan, X.-F., , and Chen, H., "Kinetic Theory Representation of Hydrodynamics: a Way Beyond the Navier-Stokes Equation," *Journal of Fluid Mechanics*, Vol. 550, 2006, pp. 413–441.

[20] Teixeira, C., "Incorporating Turbulence Models into the Lattice-Boltzmann Method," *International Journal of Modern Physics*, Vol. 9, No. 8, 1998, pp. 1159–1175.

[21] Amiet, R. K., "Noise Produced by Turbulent Flow into a Propeller or Helicopter Rotor," *AIAA Journal*, Vol. 15, No. 3, 1977, pp. 307–308.

[22] Paterson, R. W., and Amiet, R. K., "Acoustic Radiation and Surface Pressure Characteristics of an Airfoil due to Incident Turbulence," NASA CR 2733, 1976.